

High resolution millimeter imaging of the proto-planetary nebula He 3-1475^{*}

P. J. Huggins¹, C. Muthu², R. Bachiller², T. Forveille^{3,4}, P. Cox⁵

¹ Physics Department, New York University, 4 Washington Place, New York, NY 10003, USA

² IGN Observatorio Astronómico Nacional, Apartado 1143, E-28800 Alcalá de Henares, Spain

³ Observatoire de Grenoble, B.P. 53X, 38041 Grenoble Cedex, France

⁴ CFHT, PO Box 1597, Kamuela, HI 96743, USA

⁵ Institut d'Astrophysique Spatiale, Université de Paris XI, 91405 Orsay, France

Received ???; accepted ???

Abstract. We report high resolution ($1''$ – $2''$) imaging of the CO 2–1 line and the millimeter continuum in the proto-planetary nebula He 3-1475. The observations reveal the presence of a massive ($\sim 0.6 M_{\odot}$) envelope of molecular gas around the origin of the remarkable bipolar jet system seen in optical images with the *HST*. The CO kinematics are well modeled by an expanding, bi-conical envelope: the prominent, high-velocity ($\sim 50 \text{ km s}^{-1}$) wings seen in single-dish CO spectra arise where the sides of the bi-cones are projected along the line of sight. The continuum is detected at 1.3 mm and 2.6 mm and is due to thermal emission from warm ($\sim 80 \text{ K}$) circumstellar dust. The structure, kinematics, and expansion time of the envelope provide strong evidence for entrainment of the molecular gas by the high velocity jets. The observations support an evolutionary scenario in which a period of enhanced mass loss by the central star is followed by the development of the bipolar jets which burst through the molecular envelope. The jet-envelope interactions play a crucial role in shaping the subsequent ionized nebula.

Key words. Planetary nebulae: general – Planetary nebulae: individual: He 3-1475 – ISM: jets and outflows – Stars: AGB and post-AGB

1. Introduction

Collimated, bipolar outflows or “jets” are an important feature of the early evolution of planetary nebulae (PNe) that has only recently been widely recognized. Many proto-PNe and PNe are now known to show evidence of bi-polar or multi-polar structures, or point symmetries, which have been produced by the action of symmetric jets from the central star (see, e.g., Kastner et al. 2000), and these structures are sufficiently common that possibly most or all PNe pass through this phase (Sahai & Trauger 1998).

The jets are most active in the early phases of PNe formation, and their effects can be detected in proto-PNe as high velocity wings in low angular resolution, molecular line spectra of the neutral circumstellar envelopes (e.g., Cernicharo et al. 1989; Young et al. 1992; Bujarrabal et al. 2001). In the few cases observed at high angular resolution, the wings are seen to arise in directed outflows of entrained molecular gas (e.g., Cox et al. 2000, 2003). The origin of

the jets that cause the outflows is not well understood, but the jets clearly have major effects on the structure and dynamics of the neutral circumstellar envelopes from which the ionized nebulae form (Huggins et al. 1996), and consequently they play a key role in the early shaping of PNe. Well studied examples of young PNe that show evidence for interactions between the jets and the neutral circumstellar gas include BD+30°3639 (Bachiller et al. 2000), KJpN 8 (Forveille et al. 1998) and M1-16 (Huggins et al. 2000).

He 3-1475 (IRAS 17423–1755) is an extreme example of a proto-PN with highly collimated bipolar outflows, first discussed by Riera et al. (1995) and Bobrowski et al. (1995). It is of special interest because of the high velocities and remarkable structure seen in high resolution optical observations made with the HST (Borkowski et al. 1997; Borkowski & Harrington 2001; Sánchez-Contreras & Sahai 2001; Riera et al. 2003). The outflows terminate in a series of knots that are point symmetric about the central star, and indicate formation by episodic jets whose direction is time dependent.

Little is known about the neutral circumstellar matter in He 3-1475. *IRAS* fluxes indicate the presence of a circumstellar dust envelope (Parthasarathy & Pottasch 1989)

Send offprint requests to: P. J. Huggins

* Based on observations carried out with the IRAM Plateau de Bure Interferometer. IRAM is supported by INSU/CNRS (France), MPG (Germany) and IGN (Spain).

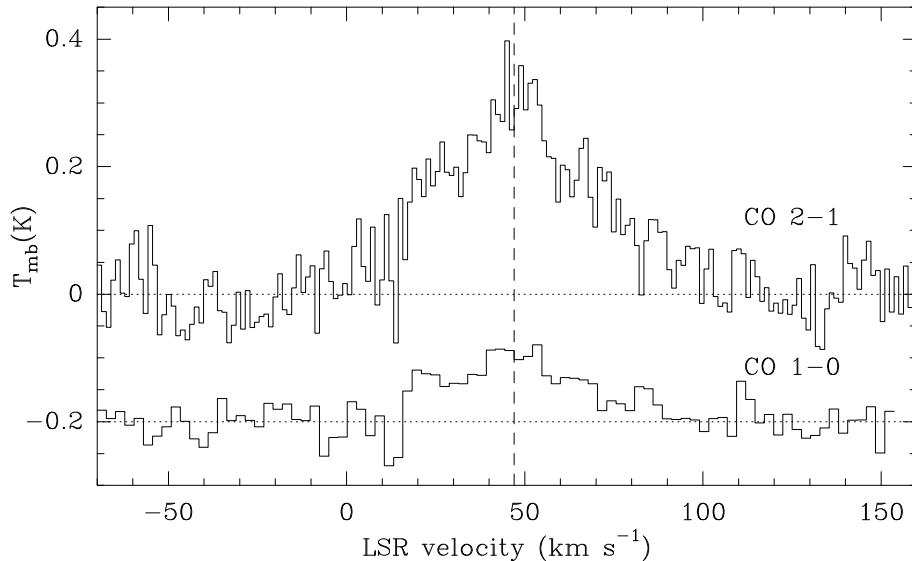


Fig. 1. CO spectra in the 1–0 (115 GHz) and 2–1 (230 GHz) lines towards He 3-1475, obtained with the IRAM 30 m telescope.

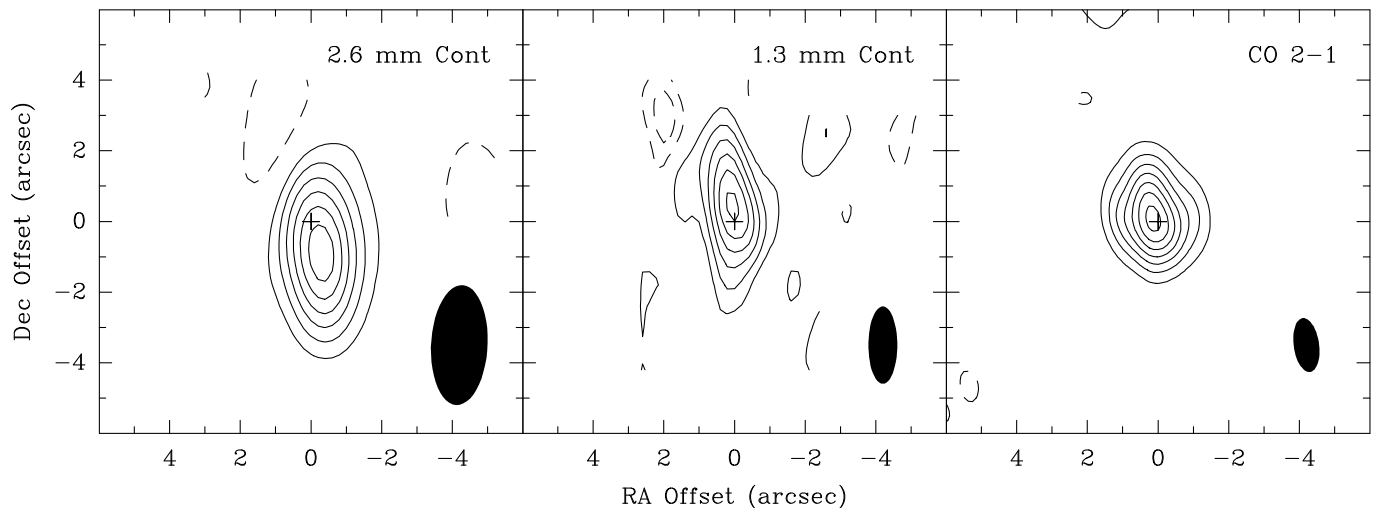


Fig. 2. Millimeter maps of He 3-1475 obtained with the IRAM interferometer. *Left:* the continuum at 2.6 mm. *Center:* the continuum at 1.3 mm. *Right:* the velocity integrated CO 2–1 line. The contour intervals are 1 mJy beam^{-1} (2.6 mm), 2 mJy beam^{-1} (1.3 mm), and 50 K km s^{-1} (CO); dashed contours are negative. The field center is $17^{\text{h}}45^{\text{m}}14^{\text{s}}.17, -17^{\circ}56'47''.0$ (J2000), and the beam size is shown in the lower right of each panel.

which is also seen in optical images as a dark lane crossing the nebular axis to the south-east of the central star. OH maser emission at 1667 MHz has been observed by te Lintel Hekkert (1991) and Bobrowski et al. (1995), and CO spectra have been reported by Knapp et al. (1995) and Bujarrabal et al. (2001). In this paper we report high angular resolution observations of the CO emission and the millimeter continuum to study the relation of the neutral circumstellar gas to the outflows.

2. Observations

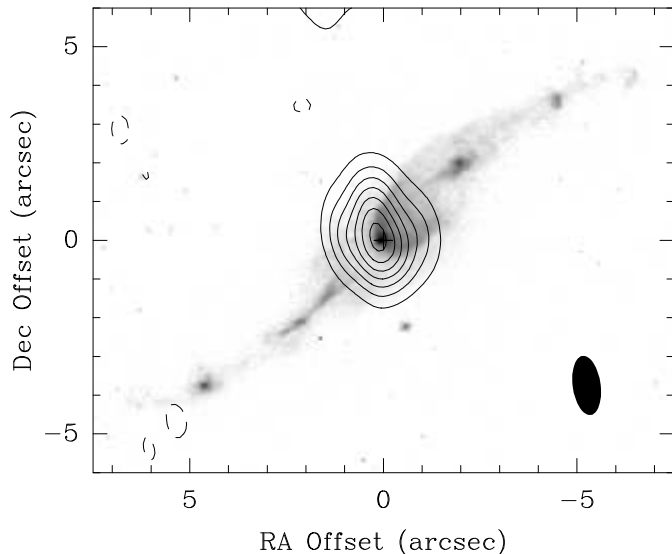
High sensitivity, single-dish observations of He 3-1475 were made in the 2.6 mm CO $J = 1 - 0$ (115 GHz) and 1.3 mm $J = 2 - 1$ (230 GHz) lines using the IRAM 30 m tele-

scope at Pico Veleta, Spain. The observations were made in September 1997, using 512×1 MHz filterbanks. The half power beam size of the telescope is $11''$ and $22''$ at the frequencies of the 2–1 and 1–0 lines, respectively. The calibration was made using the chopper wheel technique, and the line intensities are reported here as main beam brightness temperatures.

High angular resolution observations were made in the CO 1–0 and 2–1 lines and in the nearby continuum during February and March 1998 using the IRAM interferometer at Plateau de Bure, France. The array consisted of five 15 m antennas, equipped with SIS heterodyne receivers. The observations, centered on He 3-1475, were made with two configurations of the array, with baselines up to 280 m. The primary beam size of the interferometer

Table 1. CO observations of He 3-1475 made with the IRAM 30 m telescope

Line	V_0 (LSR) (km s^{-1})	ΔV (FWHM) (km s^{-1})	T_{mb} (K)	rms (K)	$\int TdV$ (K km s^{-1})	I ($\text{K km s}^{-1} \text{ arcsec}^2$)
1-0	47.5 ± 1.6	43 ± 4	0.10	0.02	4.7 ± 0.4	2580
2-1	47.5 ± 0.9	53 ± 2	0.28	0.04	15.9 ± 0.5	2180

**Fig. 3.** CO 2-1 map of He 3-1475 superposed on the HST WFPC2 image in [N II] $\lambda 6584$ (Borkowski et al. 1997). The CO contours are the same as in Fig. 2.

is $22''$ at 1.3 mm and $44''$ at 2.6 mm. The effective velocity resolution of the line observations used for the analysis is 8 km s^{-1} . The continuum observations were made at frequencies of 115.3 and 231.5 GHz, with effective bandwidths of 320 and 640 MHz, respectively.

The RF passband and amplitude were calibrated using 3C273 and the phase calibration was performed every 20 minutes using J1730-130 and J1830-210. The uv data were Fourier transformed and CLEANed, using the Clark algorithm and the restored Gaussian clean beam is $3''.4 \times 1''.6$ (PA = 177°) at 2.6 mm for both the line and continuum, and $1''.5 \times 0''.7$ (PA = 8°) and $2''.2 \times 0''.8$ (PA = 0°) at 1.3 mm for the line and continuum, respectively. The adopted field center for the maps is $17^{\text{h}}45^{\text{m}}14^{\text{s}}.17$, $-17^\circ56'47''.0$ (J2000).

3. Results

The CO 1-0 and 2-1 spectra obtained with the 30 m telescope towards He 3-1475 are shown in Fig. 1. A small map was made with $5''$ spacing around the center position, but the molecular emission was not found to be extended with respect to the telescope beam. The parameters of the lines, based on Gaussian fits to the spectra, and the corresponding line fluxes are given in Table 1.

The CO 1-0 and 2-1 lines were both detected at high angular resolution with the interferometer, and the observations recover 97% and 72% of the single-dish fluxes for the 1-0 and 2-1 lines, respectively. The observed distribution of CO is shown in the velocity integrated map of the 2-1 emission in the right hand panel of Fig. 2. The position of the peak CO emission is at $+0''.15 \pm 0''.15$, $+0''.05 \pm 0''.15$ relative to the map center, and the emission is extended with respect to the telescope beam, with a deconvolved source size of $\sim 1''.6$ (FWHM). The CO distribution is compared with the optical structure of the nebula in Fig. 3, and the CO kinematics are shown in channel maps and velocity-position maps, together with model simulations, in Figs. 4-6. The interferometer observations in the CO 1-0 line produced essentially the same results as the 2-1 observations, but with a factor of two lower resolution (because of the longer wavelength), so are not discussed further.

The millimeter continuum of He 3-1475 was detected at 1.3 mm and 2.6 mm with the interferometer, and maps of the emission are shown in the center and left hand panels of Fig. 2. At 2.6 mm the emission is not extended with respect to the telescope beam, and the measured flux is $5.3 \pm 1.2 \text{ mJy}$. At 1.3 mm the observed emission ($2''.8 \pm 0''.2 \times 1''.1 \pm 0''.4$, PA = 12°) is slightly extended with respect to the beam, and the measured flux is $31 \pm 4 \text{ mJy}$. The position of the peak emission in the 1.3 mm continuum is at $+0''.04 \pm 0''.05$, $+0''.40 \pm 0''.12$ relative to the map center, and is essentially coincident with the position of peak CO emission, within the uncertainties.

4. Properties of the envelope

4.1. Overview

The CO spectra of He 3-1475 (Fig. 1) are much broader than the $5\text{--}15 \text{ km s}^{-1}$ linewidths typically seen in AGB envelopes, and the shapes of the profiles are different. They show prominent, high velocity wings with no clear low velocity component corresponding to an undisturbed envelope: thus most or all of the molecular gas appears to participate in the high velocity flow.

From the measurements given in Table 1, the systemic LSR radial velocity (V_0) of the molecular gas is well determined to be $V_0 = 47.5 \pm 0.8 \text{ km s}^{-1}$. This corresponds to a heliocentric velocity of 34.5 km s^{-1} , and is in good agreement with the (heliocentric) velocity of $37.6 \pm 1.2 \text{ km s}^{-1}$ recently reported by Borkowski & Harrington (2001), based on five stellar lines.

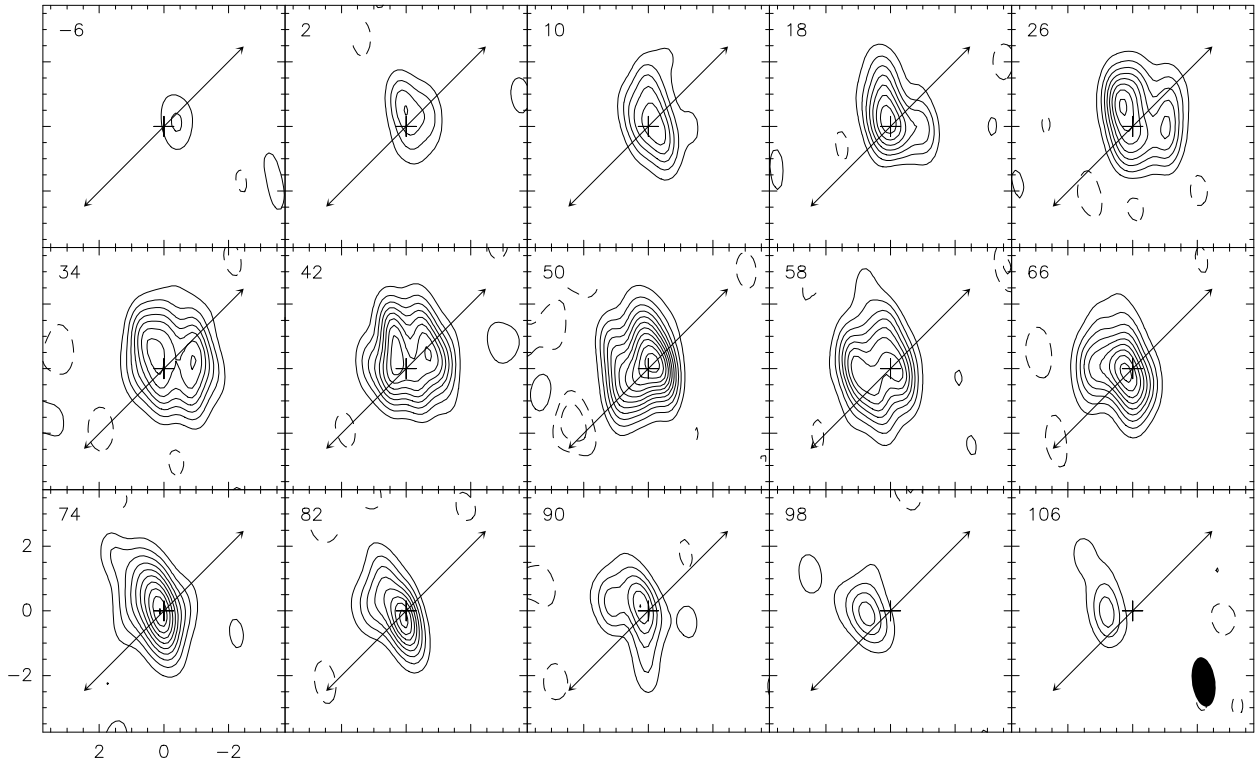


Fig. 4. Channel maps of the CO 2–1 emission observed in He 3-1475. The channels are 8 km s^{-1} wide, and are centered at the velocities given in the upper left of each panel. The contour interval is 0.5 K ; the dashed contours are negative. The arrows indicate the major (jet) axis ($\text{PA} = 135^\circ$), and the beam size is shown in the lower right panel.

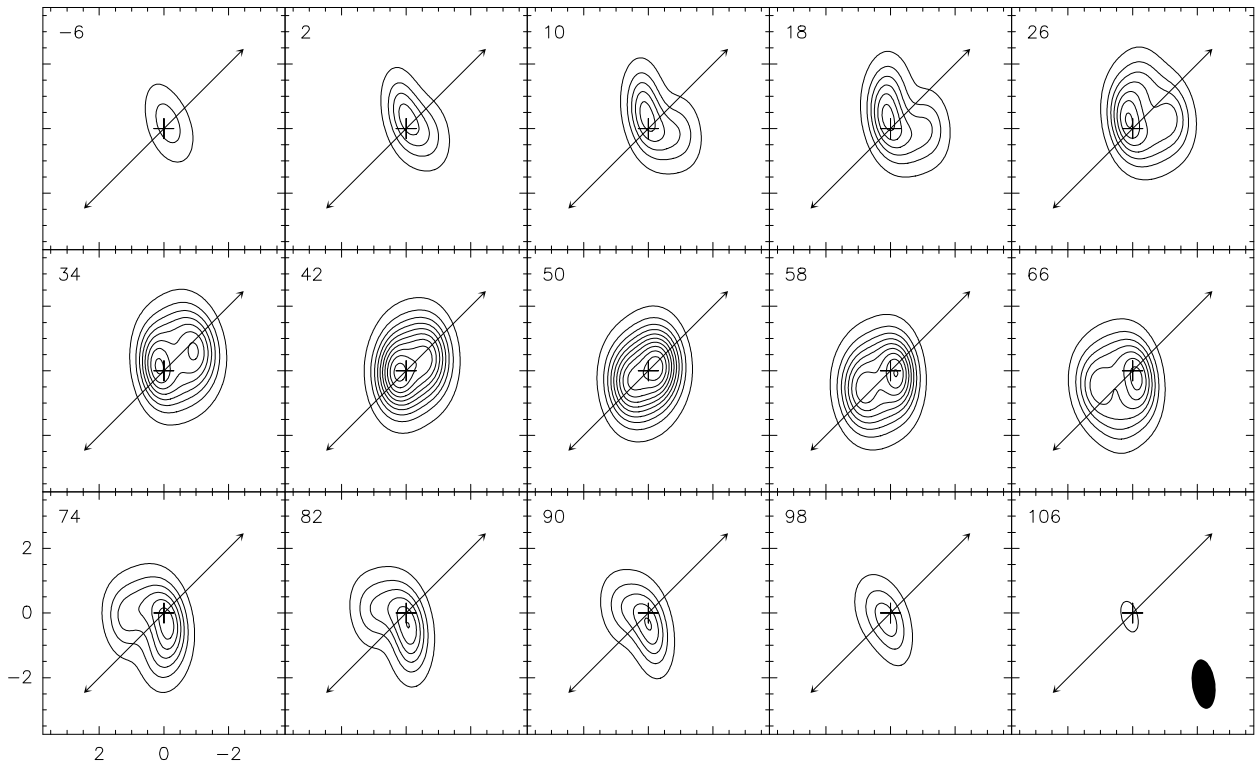


Fig. 5. Theoretical channel maps of the CO 2–1 emission for the biconical model discussed in the text. The channels are 8 km s^{-1} wide, and are centered at the velocities given in the upper left of each panel. The contours are from 5% to 95% (in steps of 10%) of the peak emission.

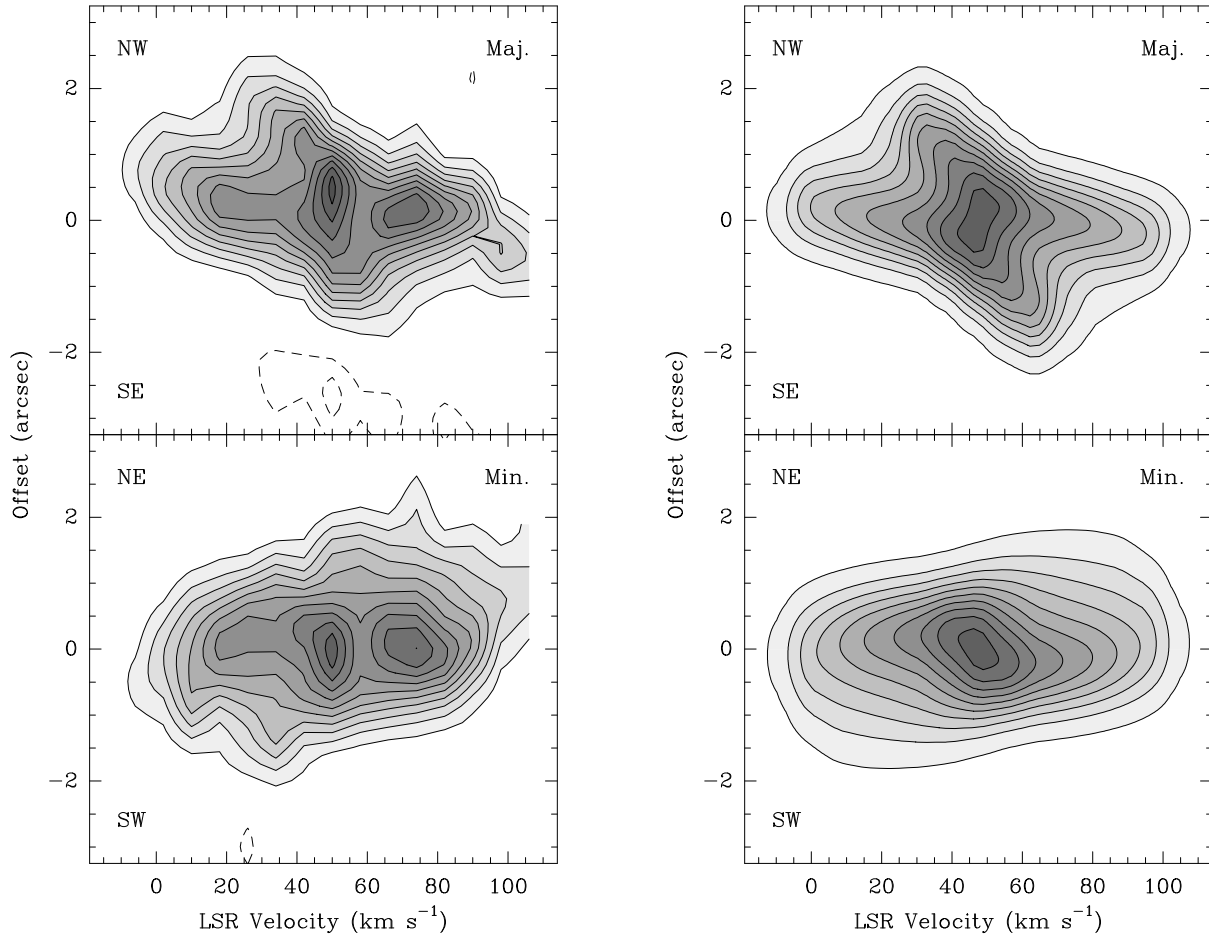


Fig. 6. Position-velocity maps of the CO 2–1 emission in He 3-1475 along the major ($PA = 135^\circ$) and minor ($PA = 45^\circ$) axes. *Left*: observed data; the contour interval is 0.5 K; dashed contours are negative. *Right*: theoretical maps for the biconical model discussed in the text. The contours are from 5% to 95% (in steps of 10%) of the peak emission.

The comparison of the CO map and the HST WFPC2 image in $[\text{N II}] \lambda 6584$ (Borkowski et al. 1997) in Fig. 3 shows that the CO emission peaks close to the center of the nebula, but is quite limited in extent compared to the optical image. The molecular emission covers the central dark lane and extends out along the opening of the bipolar structure, but does not envelop the extended, collimated jet system. The characteristic radius of the CO map ($0''.8$) corresponds to 7×10^{16} cm at a distance of 5.8 kpc, which we adopt for the distance to He 3-1475 (Riera et al. 2003).

4.2. CO kinematic structure

Although the CO emission is not very extended with respect to the telescope beam, the velocity-resolved CO observations provide insights into the overall kinematic structure of the molecular gas. The complete data cube is shown in Fig. 4 in the form of channel maps. These exhibit an approximate position-velocity symmetry about the central position and velocity, e.g., the emission in the extreme blue shifted channels (at -6 , $+2$, and $+10$ km s^{-1}) is offset to the NW of the field center and that of the extreme red channels ($+90$, $+98$ and $+106$ km s^{-1}) is offset

to the SE. The maps also exhibit a rough axial symmetry about the major axis of the optical nebula (the jet axis) at $PA = 135^\circ$, although the CO intensities are affected by the shape of telescope beam, which is elliptical and lies at an angle of 53° with respect to the nebula axis. Thus the arc-like features in blue channels $+10$ and $+18$ km s^{-1} and red channels $+82$ and $+90$ km s^{-1} , which point away from the center, appear stronger where the emission lies along the primary axis of the beam (see §4.3 below).

The velocity-position maps through the data cube along the major and minor axes shown in Fig. 6, demonstrate that the whole CO structure is tilted toward us (blue shifted) to the NW and away from us (red shifted) to the SE along the major axis. This tilt is in the same sense as that of the optical bipolarity and jets (e.g., Riera et al. 2003). In addition, the distribution of intensity in the map along the major axis indicates that the molecular gas forms an expanding, open ended, bi-conical structure that can also be traced in the channel maps in Fig. 4. Thus the extreme, blue shifted emission (in channels -6 and $+2$ km s^{-1}) arises in the lower rim of the cone facing toward us; this rim lies nearly in the direct line of sight, and gives rise to the highest blue shifted gas seen in the wings

of the single dish spectra. At intermediate, blue shifted channels ($10\text{--}26\text{ km s}^{-1}$), the arc-like structure becomes more prominent as the channel includes a larger cross section of the cone, and closer to the systemic velocity (at $+42\text{ km s}^{-1}$) the channel also includes the upper rim of the cone. At red shifted channels, the overall symmetry is reversed for the cone facing away from us.

4.3. Model of the CO kinematics

In order to quantify our interpretation of the CO data, we have constructed a simple, biconical model of the CO emission for comparison with the observations. The model is characterized by the radius at the equator where the cones intersect (R_i), the radius of the open ends (R_o), the height of each cone (h), and the inclination of the symmetry axis to the line of sight (i). We assume a constant thickness (t), and a relative density within the cones that varies as a power law from the center ($\rho \sim r^n$). The emission is taken to be optically thin (see below), and the expansion is assumed to be homologous, with the radial velocity $v \sim r$. This velocity law is motivated by the observed structure in the data cube, and by similar ballistic flows seen in other proto-PNe (e.g., AFGL 618, Cox et al. 2003).

From comparison with the observations, the parameters of a best-fit model are $R_i = 0''.45$, $R_o = 0''.92$, $h = 1''.5$, $t = 0''.5$, $n = -0.5$, $i = 40^\circ$, and a velocity gradient of $31.4\text{ km s}^{-1}\text{ arcsec}^{-1}$. The linear dimensions are given in arc seconds on the sky, since they scale with distance. The thickness of the walls of the bicones is not actually resolved by the observations, and is set to a nominal value. The parameter n is constrained by the relative intensity of the extended CO emission to that near the center, and the dimensions of the bicones, the velocity gradient, and the inclination are jointly constrained by the map sizes at different velocities, and the relative projections of the sides of the cones in the position-velocity map. For example, a general constraint on the inclination and the opening angle of the bicones is provided by the major axis position-velocity map, where the blue shifted, lower rim of the cone facing toward us is very close to the line of sight, and the upper rim is also blue shifted. In this case, the inclination angle of the symmetry axis $i \lesssim 45^\circ$ and the opening angle of the cone from the center is $\lesssim 45^\circ$ (otherwise the upper rim would be red shifted). Similarly the inclination cannot be much less than $\sim 40^\circ$ or the upper rim would project to higher velocities than are observed.

The results of the best-fit model are shown in Fig. 5 and Fig. 6 (right panel). In spite of the extreme simplicity of the model, it can account for the main features of the observations. The inclination of the CO bicones to the line of sight is essentially the same as that of the optical jets (Borkowski & Harrington 2001), and the biconical geometry indicates that molecular gas lies around the base of the jet flows. As noted above we do not resolve the walls of the bicones, but the parameter n together with

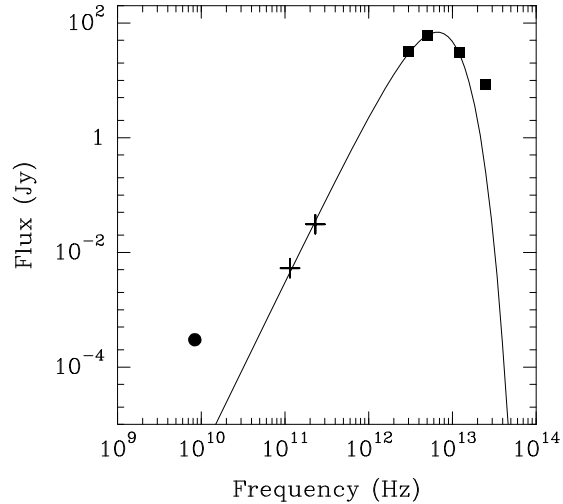


Fig. 7. The infrared–radio spectrum of He3-1475. The flux measurements are from IRAS (squares), this paper (crosses), and Knapp et al. (1995) (circle). The smooth curve is for thermal emission from dust at a temperature of 81 K.

the assumed constant wall thickness determines the mass distribution in the bicones: for the solution $n = -0.5$, the mass per unit length projected along the major axis is approximately constant, which is reasonable for such a flow.

The kinematic model is axi-symmetric but our calculations of the simulated observations also include the elliptical telescope beam which is not aligned along this axis. The effects can be seen in Figs. 5 and 6. They include the asymmetries in intensity of the arc-like features in the channel maps noted earlier, and a more subtle effect in a shift from red to blue (from NE to SW) in the minor axis position-velocity map, which is also apparent in the real data. Two features of the observations are not reproduced by the model simulations. The first is a slight channel-to-channel shift in the position of the emission at high velocities, and this could be accommodated by some degree of curvature in the sides of the bicones. The second is slightly higher equatorial emission in the observations than in the model, which could be accommodated by higher densities or a modified geometry near the equator. However, the emission is probably at least partially thick, especially near the equator, and we have not included this in the simple model, so fine tuning with additional parameters would be unwarranted. Nevertheless, independent of optical depth effects, the basic kinematic structure is well accounted for by the simple model.

4.4. The circumstellar dust component

Our millimeter continuum observations fill a large gap in the observed long wavelength spectrum of He 3-1475, and they provide an estimate of the mass of circumstellar dust. As shown in Fig. 7, the only other long wavelength observations of He 3-1475 are from *IRAS*, and a single radio observation at 3.6 cm. The centimeter continuum is likely

to be free-free emission from the compact ionized core, and from comparison with the flux in H α Borowski et al. (1995) suggest that the emission is optically thick. An optically thick radio spectrum which varies as ν^2 does not, however, extend into the millimeter region because the 115 GHz (2.6 mm) flux would then be much higher than we observe. The free-free emission spectrum likely becomes optically thin and levels off between 10 and 100 GHz.

The millimeter flux increases quite steeply with increasing frequency, and from the overall shape of the spectrum the main contribution to the observed 1.3 mm and 2.6 mm flux is probably the long wavelength tail of the dust emission seen in the infrared. This is supported by the fact that we are able to simultaneously provide a good fit to the 25–100 μm (color corrected) *IRAS* fluxes and to the observed millimeter fluxes, with a single temperature dust component. Formal fits, varying both the temperature and the index of dust emissivity p (where $Q(\nu) \sim \nu^p$), give $T_d = 81 \pm 4$ K, and $p = 0.99 \pm 0.07$.

With this value for the temperature, we estimate the mass of the cool dust component using the optically thin expression $M_d = F_\nu D^2 / (\chi_\nu B_\nu(T))$, where F_ν is the flux, χ_ν the emissivity per unit mass, and B_ν the Planck function at frequency ν , and D is the distance. Using the *IRAS* flux at 60 μm , $\chi_{60} = 150 \text{ cm}^2 \text{ g}^{-1}$ (Jura 1986), and $D = 5.8$ kpc, we find $M_d = 6.4 \times 10^{-3} M_\odot$. A second component with a higher temperature and a much smaller mass, which we ignore, can account for the additional, short wavelength emission in the spectrum in Fig. 7.

4.5. Mass of circumstellar gas

The mass of circumstellar gas can be estimated from the dust mass given above, by adopting a value for the gas-to-dust ratio. For transition objects with high mass loss rates, the gas-to-dust ratio appears to be somewhat smaller than for typical AGB stars, and we adopt the value of ~ 100 from Knapp et al. (1993). This yields a mass of circumstellar gas $M_g = 0.64 M_\odot$.

The CO observations provide a second estimate for the mass of circumstellar gas. In this case, it is a lower limit because the low (~ 0.9) CO 2–1/1–0 flux ratio (Table 1) suggests that the CO lines may be at least partially optically thick, although an alternative possibility is that the CO is sub-thermally excited. In any event we obtain a lower limit to the mass of molecular gas using the optically thin formula given by Huggins et al. (1996). For a distance of 5.8 kpc and a representative CO/H₂ abundance of 2×10^{-4} which is commonly assumed for oxygen-rich envelopes (e.g., Kahane & Jura 1994), we find $M_g \gtrsim 0.19 M_\odot$, consistent with the estimate given above.

These values are in accord with a further estimate of the mass of circumstellar gas, given by Bujarrabal et al. (2001) based on observations of the ¹³CO lines. This approach minimizes the effect of line opacity because the lines are likely to be optically thin, but relies on an assumed value for the ¹³CO/H₂ abundance. For their as-

sumed value (2×10^{-5}), and our adopted distance of 5.8 kpc to He 3-1475, $M_g = 0.85 M_\odot$, consistent with the above values.

5. Jet-envelope interactions

Our observations of the molecular emission in He 3-1475 support an evolutionary scenario in which a period of enhanced mass loss by the central star is followed by the development of bipolar jets that burst through the surrounding molecular gas.

5.1. Mass loss rate of the precursor

The current mass of circumstellar molecular gas around He 3-1475 is substantial (§4.5), and it was presumably ejected by the star at a moderate velocity characteristic of the AGB. For a velocity of $\sim 15 \text{ km s}^{-1}$, the size of the CO map that we observe (§3) implies an ejection time scale of $\lesssim 1,500$ yr, and a corresponding mass loss rate over this time of $\gtrsim 1.3 \times 10^{-4} M_\odot \text{ yr}^{-1}$, using our lower limit on the CO mass. This mass loss rate is much larger than typically seen on the AGB, but is characteristic of some other transition objects (e.g., AFGL 2688, Jura et al. 2000), and is either an intrinsic part of the final evolution of single stars on the AGB, or the result of binary interactions.

5.2. Envelope entrainment

In addition to enhanced mass loss, the kinematics and structure of the circumstellar gas indicate that most or all of the molecular envelope has been affected by recent interaction with the jets. First, the CO velocities (up to $\sim 50 \text{ km s}^{-1}$) are significantly larger than the expansion velocities of AGB stars, but are much less than velocities seen in the ionized gas close to the jet axes (Borkowski & Harrington 2001; Sánchez-Contreras & Sahai 2001; Riera et al. 2003). Second, the observations show that the molecular gas forms an expanding bi-conical structure around the base of the optical bipolar flows. Thus both the structure and kinematics provide strong evidence for entrainment of the molecular gas.

The kinematic time scales support this view. From proper motion studies using HST, the expansion time scales (r/v projected on the plane of the sky) of the ionized knots at $\pm 6''$ from the center are $\tau_{\text{exp}} \sim 450\text{--}550$ yr, and for the most distant knots at $\pm 7''5$, $\tau_{\text{exp}} \sim 600$ yr (Riera et al. 2003; Borkowski & Harrington 2001). For comparison, the kinematic time scale of the molecular gas is obtained by combining the (angular) velocity gradient of our kinematic model (§4.3) and the adopted distance of 5.8 pc, which give $\tau_{\text{exp}} \sim 875$ yr. Thus the CO outflows and the earliest jets are comparable in age.

There are large velocity gradients from the axes of the jets to the sides of the CO bicones, as expected if the jets burst through the envelope. The maximum CO velocity that we observe is $\sim 50 \text{ km s}^{-1}$, which is in fact close to

the maximum velocity for molecular gas to survive acceleration in a single shock (Draine et al. 1983), although it is possible for molecules to reform at higher velocities in post-shocked gas (Hollenbach & McKee 1989; Neufeld & Dalgarno 1989). Details of the interaction need further study, but it seems likely that much of the fast, ionized material seen in the optical outflows has been produced by the destruction of molecules in the entrainment process. Similarly, there may also be an intermediate component of neutral atomic gas produced by the interactions which could be detected in species such as C II, C I, and O I.

Molecular H₂ has been detected in the axial knots themselves (Harrington et al. 2000). This is probably at very high velocity (although no spectroscopy has yet been done) and the emission is likely formed in dense, post-shocked gas, possibly under conditions similar to those in AFGL 618 discussed by Cox et al. (2003).

Weak OH maser emission has also been observed toward He 3-1475 (te Lintel Hekkert 1991; Bobrowski et al. 1995) and is distributed in multiple maser spots within $\sim 0''.8$ of the center, with a velocity range $\sim 20\text{--}75\text{ km s}^{-1}$, roughly centered on the CO systemic velocity. The kinematic structure of the OH masers in Fig. 5 of Bobrowski et al. (1995) appears to show a strong velocity gradient across the envelope which has been remarked on by others, e.g., Riera et al. (2003). This apparent gradient is, however, not real. It is an artifact of ascribing positive and negative radial offsets to the red and blue components, and the actual distribution of the maser components shows no clear cut geometry (Zijlstra et al. 2001). Given the OH maser velocities, the spots are probably located in the inner regions of the CO bicones near the equatorial plane.

5.3. Envelope dynamics

It has long been suspected that stellar radiation pressure may not power the highest mass loss rates in post-AGB stars (e.g., Knapp et al. 1982), and recent survey work by Bujarrabal et al. (2001) has quantified this for the molecular outflows seen as high velocity wings in single dish CO spectra. We follow their approach in estimating the linear momentum (P) and energy (E) of the outflow using the observed values along the line of sight, and correcting for the inclination. We use the position-velocity map of Fig. 6 to define the outflow as the emission at velocities $|V - V_0| > 5\text{ km s}^{-1}$. For $d = 5.8\text{ kpc}$ and $i = 40^\circ$ adopted earlier, we find $P \gtrsim 1 \times 10^{39}\text{ g cm s}^{-1}$ and $E \gtrsim 2 \times 10^{45}\text{ erg}$ using the CO emission. If we use the mass estimate based on the millimeter continuum and assume a velocity distribution as in the CO profile, the actual values are ~ 3 times larger than these limits. The results are similar to those obtained by Bujarrabal et al. (2001) for He 3-1475, based on the ¹³CO lines.

The luminosity of He 3-1475 at a distance of 5.8 kpc is $L = 12,600 L_\odot$ (Riera et al. 2003). If radiation pressure from the star drives the molecular outflows, the time scale to generate the observed momentum (defined by the

equation $\tau(L/c) = P$) is $\gtrsim 2 \times 10^4\text{ yr}$. However, as discussed in §5.2, the CO expansion time is only $\sim 875\text{ yr}$, and the actual time to accelerate the molecular gas to the observed velocities is probably less. Thus radiation pressure is unable to drive the flow by a large margin, as found by Bujarrabal et al. (2001) for more than 20 cases. This result is not unexpected in He 3-1475 because the geometry and kinematics discussed above provide strong evidence that the molecular gas is accelerated by entrainment in the jets, and these highly collimated structures are not likely generated by radiation pressure.

In He 3-1475 the jets appear to have easily penetrated the dense circumstellar gas close to the star: the molecular gas is peripheral to the outflows, and is at relatively low velocities compared to the jet axes. In these circumstances, it might be expected that the energy and momentum of the flow estimated from the molecular gas alone would be a relatively small part of the total, i.e., that the values given above are strong lower limits. It is therefore surprising that the energy and momentum in the fast outflows estimated by Riera et al. (2003) from optical observations are $P \sim 10^{37}\text{ g cm s}^{-1}$ and $E \sim 10^{45}\text{ erg}$, which are *less* than the values we estimate from the molecular emission, the value of P less by a factor of 100.

This discrepancy requires explanation and we offer two solutions. One is that the material close to the jet axes is largely neutral. Riera et al. (2003) have estimated the flow parameters based on a density determined from [S II] line ratios. If the material is largely neutral, as expected from calculations of jets in YSOs (e.g., Safier 1993; Shang et al. 2002), then the actual densities could be much larger, and the dynamical quantities correspondingly higher. A second possibility is that the primordial jets are in fact components of a wide angle wind. If so, the wide angle wind might couple well to the molecular gas, with only the central, highest velocity material breaking through the envelope to form the visible jets. These scenarios need to be examined in other proto-PNe.

6. Conclusions

The millimeter observations reported here provide basic information on the properties of the neutral circumstellar matter around the remarkable proto-planetary nebula He 3-1475. The observations also underscore the importance of neutral circumstellar gas in the early development of PNe.

He 3-1475 is surrounded by a massive circumstellar envelope ($\gtrsim 0.2 M_\odot$ and $\sim 0.6 M_\odot$ from our CO and continuum observations, respectively), which has only recently been ejected by the central star at a high mass loss rate ($\gtrsim 1 \times 10^{-4} M_\odot \text{ yr}^{-1}$). The structure and kinematics of the CO emission are well modeled with an expanding bi-conical envelope, and lead to the conclusion that the molecular gas has been entrained in the sides of the jets as they burst through the envelope. The expansion time scales of the CO emission and the jets support this view.

Although He 3-1475 is an extreme object on account of the very high velocity of the jets and its well developed point symmetric structure, the evolutionary scenario outlined above is very similar to other newly forming PNe we have studied at high resolution. AFGL 2688 (Cox et al. 2000), CRL 618 (Cox et al. 2003); M1-16 (Huggins et al. 2000), KJPN 8 (Forveille et al. 1998), and NGC 7027 (Cox et al. 2002) form an approximate evolutionary sequence in which the ionized nebula turns on and becomes more dominant, and in each case there are prominent multiple jets, or single jets which have changed direction. He 3-1475 clearly belongs with this class. Besides constraining the origin of the jets and the physics of jet-envelope interactions, the observations of these objects demonstrate the importance of jets in the early shaping of the neutral circumstellar envelopes which play a key role in determining the morphology of the mature PNe.

Acknowledgements. We thank Drs. M. Bobrowski, J. P. Harrington, and A. Zijlstra for useful discussions, and J. P. Harrington for the image used in Fig. 3. We also thank the IRAM staff at Plateau de Bure for making the observations, and the staff at Grenoble for help with the data. This work was supported in part by NSF grants AST 99-86159 and AST 03-07277 (to P.J.H.) and the Spanish DGES grant AYA2000-927 (to R.B.).

References

- Bachiller, R., Forveille, T., Huggins, P. J., Cox, P., & Maillard, J. -P. 2000, *A&A*, 353, L5
- Bobrowski, M., Zijlstra, A. A., Grebel, E. K., et al. 1995, *ApJ*, 446, L89
- Borkowski, K. J., Blondin, J. M., & Harrington, J. P. 1997, *ApJ*, 482, L97
- Borkowski, K. J., & Harrington, J. P. 2001, *ApJ*, 550, 778
- Bujarrabal, V., Castro-Carrizo, A., Alcolea, J., & Sánchez Contreras, C. 2001, *A&A*, 377, 868
- Cernicharo, J., Guélin, M., Penalver, J., Martín-Pintado, J., & Mauersberger, R. 1989, *A&A*, 222, L1
- Cox, P., Lucas, R., Huggins, P. J., et al. 2000, *A&A*, 353, L25
- Cox, P., Huggins, P. J., Maillard, J. -P., et al. 2002, *A&A*, 384, 603
- Cox, P., Huggins, P. J., Maillard, J. -P., et al. 2003, *ApJ*, 586, L87
- Draine, B. T., Roberge, W. G., & Dalgarno, A. 1983, *ApJ*, 264, 485
- Forveille, T., Huggins, P. J., Bachiller, R., & Cox, P. 1998, *ApJ*, 495, L111
- Harrington, J. P., & Borkowski, K. J. 2000, in *Asymmetrical Planetary Nebulae II: From Origins to Microstructures*, ed. J. H. Kastner, N. Soker, & S. Rappaport, ASP Conf. Ser., 199, 383
- Hollenbach, D., & McKee, C. F. 1989, *ApJ*, 342, 306
- Huggins, P. J., Bachiller, R., Cox P., & Forveille, T. 1996, *A&A*, 315, 284
- Huggins, P. J., Forveille, T., Bachiller, R., & Cox, P. 2000, *ApJ*, 544, 889
- Jura, M. 1986, *ApJ*, 303, 327
- Jura, M., Turner, J. L., Van Dyk, S., & Knapp, G. R. 2000, *ApJ*, 528, L105
- Kahane, C., & Jura, M. 1994, *A&A*, 290, 183
- Kastner, J. H., Soker, N., & Rappaport, S. 2000, *Asymmetrical Planetary Nebulae II: From Origins to Microstructures*, ed. J. H. Kastner, N. Soker, & S. Rappaport, ASP Conf. Ser., 199
- Knapp, G. R., Phillips, T. G., Leighton, R. B., et al. 1982, *ApJ*, 252, 616
- Knapp, G. R., Sandell, G., & Robson, E. I. 1993, *ApJS*, 88, 173
- Knapp, G. R., Bowers, P. F., Young, K., & Phillips, T. G. 1995, *ApJ*, 455, 293
- Neufeld, D. A., & Dalgarno, A. 1989, *ApJ*, 340, 869
- Parthasarathy, M., & Pottasch, S. R. 1989, *A&A*, 225, 521
- Riera, A., Garcia-Lario, P., Machado, A., Pottasch, S. R., & Raga, A. C. 1995, *A&A*, 302, 137
- Riera, A., Garcia-Lario, P., Machado, A., Bobrowsky, M., & Estalella, R. 2003, *A&A*, 401, 1039
- Safier, P. 1993, *ApJ*, 408, 115
- Sahai R., & Trauger J. T. 1998, *AJ*, 116, 1357
- Sánchez Contreras, C., & Sahai, R. 2001, *ApJ*, 553, L173
- Shang, H., Glassgold, A. E., Shu, F. H., & Lizano, S. 2002, *ApJ*, 564, 853
- te Lintel Hekkert, P. 1991, *A&A*, 248, 209
- Young, K., Serabyn, G., Phillips, T. G., et al. 1992, *ApJ*, 385, 265
- Zijlstra, A. A., Chapman, J. M., te Lintel Hekkert, P., et al. 2001, *MNRAS*, 322, 280